Error estimation in multitemporal InSAR deformation time series, with application to Lanzarote, Canary Islands

Pablo J. González[1,2] and José Fernández[1,3]

Received 1 April 2011; revised 7 July 2011; accepted 19 July 2011; published 13 October 2011.

[1] Interferometric Synthetic Aperture Radar (InSAR) is a reliable technique for measuring crustal deformation. However, despite its long application in geophysical problems, its error estimation has been largely overlooked. Currently, the largest problem with InSAR is still the atmospheric propagation errors, which is why multitemporal interferometric techniques have been successfully developed using a series of interferograms. However, none of the standard multitemporal interferometric techniques, namely PS or SB (Persistent Scatterers and Small Baselines, respectively) provide an estimate of their precision. Here, we present a method to compute reliable estimates of the precision of the deformation time series. We implement it for the SB multitemporal interferometric technique (a favorable technique for natural terrains, the most usual target of geophysical applications). We describe the method that uses a properly weighted scheme that allows us to compute estimates for all interferogram pixels, enhanced by a Montecarlo resampling technique that properly propagates the interferogram errors (variance-covariances) into the unknown parameters (estimated errors for the displacements). We apply the multitemporal error estimation method to Lanzarote Island (Canary Islands), where no active magmatic activity has been reported in the last decades. We detect deformation around Timanfaya volcano (lengthening of line-of-sight ~ subsidence), where the last eruption in 1730–1736 occurred. Deformation closely follows the surface temperature anomalies indicating that magma crystallization (cooling and contraction) of the 300-year shallow magmatic body under Timanfaya volcano is still ongoing.

Citation: González, P. J., and J. Fernández (2011), Error estimation in multitemporal InSAR deformation time series, with application to Lanzarote, Canary Islands, *J. Geophys. Res.*, *116*, B10404, doi:10.1029/2011JB008412.

1. Introduction

[2] Two-pass differential interferometric synthetic aperture radar (DInSAR) has emerged, together with the Global Positioning System, as the most operative geodetic tools for ground deformation monitoring due to tectonic and volcanic activity in the last two decades [*Massonnet et al.*, 1993; *Dzurisin*, 2007]. Differential InSAR provides high resolution ground deformation ($\underline{u}$) at regional level, along the line-of-sight direction ($\underline{l}$) between the satellite antenna and the imaged ground surface. DInSAR exploits the phase difference between two time-separated complex SAR images acquired under similar geometric conditions. The interpretation of simple pairwise DInSAR results has led to an impressively long list of discoveries in volcanic and tectonic deformation processes [*Massonnet et al.*, 1993, 1995; *Peltzer et al.*, 1996; *Amelung et al.*, 2000; *Fialko et al.*, 2005; *Amelung et al.*, 2007].

[3] Successful geophysical applications of classical differential InSAR have started from avoiding error quantification [*Massonnet et al.*, 1995; *Fialko and Simons*, 2001] to gradually incorporate some error assessment [*Simons et al.*, 2002; *Knospe and Jonsson*, 2010]. Several authors have suggested how to incorporate estimated observational errors for the extraction of geophysical parameters (magma volume, earthquake source parameters, etc.) [*Lohman and Simons*, 2005; *Dawson and Tregoning*, 2007; *Sudhaus and Jonsson*, 2009]. However, routine error assessment in interferometric processing methods has only been proposed in quasi-static displacement maps through classical DInSAR, and only envisaged with advanced methods [*Emardson et al.*, 2003].

[4] Advanced or multitemporal interferometric methods have been developed to overcome (1) temporal decorrelation [*Zebker and Villasenor*, 1992] and (2) atmospheric disturbances [*Zebker et al.*, 1997; *Hanssen et al.*, 1999]. Multitemporal techniques have been tested to resolve small strain rates (~1 mm/yr/10 km). The simplest, yet most effective form of advanced methods is interferogram *stacking* [*Lyons and Sandwell*, 2003; *Fialko and Simons*, 2000]. It consists in (weighted) average interferograms to enhance

[1]Instituto de Astronomía y Geodesia, CSIC-Universidad Complutense de Madrid, Madrid, Spain.
[2]Now at Department of Earth Sciences, University of Western Ontario, London, Ontario, Canada.
[3]Now at Instituto de Geociencias, CSIC-Universidad Complutense de Madrid, Madrid, Spain.

0148-0227/11/2011JB008412

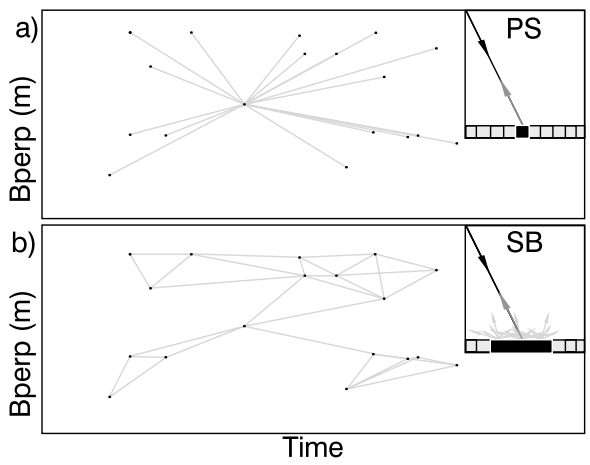

Figure 1. Advanced interferometric methods (PS versus SB). (a) PS is based on the analysis of point-like reflectors, (b) meanwhile SB exploits spatial average of distributed scatterers.

deformation detection, assuming that the error behaves as a temporal white noise process. Theoretically, it reduces errors as $\sigma = 1/\sqrt{n}$, where n is the number of independent interferograms [*Strozzi et al.*, 2001]. However, the use of stacking is limited to the study of static or temporal constant rate deformation processes. In the late Nineties, the identification that some interferogram elements remained coherent in less favorable interferometric pairs was used to overcome some of the aforementioned problems [*Usai*, 1997; *Usai and Hanssen*, 1997; *Hanssen and Usai*, 1997]. It enabled the temporal analysis of coherent/stable scatterers in a set of SAR images. Two distinct main methods have been developed: (1) *Permanent* or *Persistent Scatterer* Interferometry - PS (Figure 1a), which uses the equivalence between radar amplitude and phase stability to identify such stable elements [*Ferretti et al.*, 2000; *Hooper et al.*, 2004, 2007]. Usually, phase history is reconstructed with reference to a single image (master) and considering an a priori temporal ground deformation model (e.g. linear, sinusoidal,..). Such methods have been mainly, but not only, applied to urban areas, where such point-like scatterer mechanisms are dominant. (2) A second group of methods is the *Small Baseline* - SB (Figure 1b), which exploits small baseline interferograms to minimize the effects of baseline decorrelation and topographic errors [*Lundgren et al.*, 2001; *Berardino et al.*, 2002; *Mora et al.*, 2003; *Schmidt and Bürgmann*, 2003; *Usai*, 2003; *Lanari et al.*, 2004]. Temporal decorrelation is minimized by using short-temporal separation between acquisitions. Phase analysis is primarily done in the spatial two-dimensional space and stable distributed scatterers can be selected with spatial or temporal coherence criteria [*Berardino et al.*, 2002; *Mora et al.*, 2003; *Tizzani et al.*, 2007]. Such distributed scatterers are more frequently found in natural terrains. Finally, hybrid methods have been recently proposed to identify and exploit the phase of mixed scatterers [*Hooper*, 2008].

[5] In current advanced interferometric techniques, error estimation in the unknown parameters, namely LOS deformation (u_{los}), rely largely on the root-mean square of a certain stable area, some coherence-based errors or a combination of both [*Hooper et al.*, 2004; *Kwoun et al.*, 2006; *Andersohn et al.*, 2009]. Therefore, an error estimation method for advanced interferometric techniques is necessary for the correct assessment of any detected deformation and its temporal evolution. Here, we formulated a rigorous Gauss-Markov mathematical model, modifying the SB multitemporal interferometric method to account for the description and analysis of the observational errors to construct a suitable observation variance-covariance matrix ($\Sigma_{\varphi\varphi}$). The new multitemporal interferometric model also take into account the inherent data correlation of SB methods when SAR acquisitions are used multiple times. For the final uncertainty refinement, we used a resampling bootstrap method. Later on, the method is validated against some simulation tests. Finally, the method is applied to the volcanic island of Lanzarote.

2. Differential InSAR Phase and Phase Errors: Theory

[6] Before describing the proposed method, we must first review the process to obtain the differential phase and the assumptions we made, as well as the properties of the error sources affecting the differential interferometric phase (σ^2_{φ}) and how we quantify their contributions.

[7] First, we aligned all available SAR acquisitions to a single master. We chose the master image based on the cumulative correlation model or total correlation [*Hooper et al.*, 2007; *Perlock et al.*, 2008]. This step tends to minimize errors related with the coregistration of long spatial baselines, although it can be somehow alleviated if a DEM-assisted coregistration is performed [*Fornaro et al.*, 2005]. Once all images have been resampled to a common master-coordinate system, interferograms are selected based on temporal and perpendicular baseline thresholds. Careful attention should be paid if the selection procedure results in a single subset or multiple subsets of short-baselines interferograms. Both options are valid but different assumptions should be made to solve the problem, as a displacement minimum norm solution or a velocity minimum norm solution respectively are needed [*Usai*, 2003; *Berardino et al.*, 2002]. Interferometric phase (ψ) has geometric contributions (flat earth and topographic phases), which have to be removed to lead to the wrapped differential phase (φ). Finally, for the later analysis the phase is unwrapped in 2D.

[8] Differential phase errors come from a variety of sources and have been previously discussed [*Hanssen*, 2001]. Here, we review source errors and the adapted solution to remove or quantify them for subsequent integration in the stochastic model of the proposed method.

2.1. Decorrelation

[9] Interferometric decorrelation is computed as a complex cross-correlation index between two complex SAR images, often referred to as its complementary coherence (ρ). Thus, coherence serves as a phase quality parameter that measures the phase stability of the target ground (ψ_{scat}), routinely calculated as a spatial approximation (multilooked) [*Hanssen*, 2001]. Broadly speaking, decorrelation in interferograms occurs as the combination of several processes, namely the temporal, processing, geometric, doppler-centroid, volumetric and thermal decorrelations [*Massonnet and Feigl*, 1998;

Hanssen, 2001; *Simons and Rosen*, 2007, and references therein]. *Zebker and Villasenor* [1992] demonstrated that decorrelation effects are multiplicative and a total coherence value accounts for all decorrelation phase error sources.

[10] So, if we consider that our SAR system is imaging a natural terrain and among any possible reflection mechanisms, distributed scatterers would be predominant [*Curlander and McDonough*, 1991]. A common approach for estimating the standard deviation of the interferometric phase is assuming that within a given interferogram pixel, reflections can be modeled as the sum of many randomly and independently oriented subreflectors (Figure 1b, inset). If no single reflector dominates the radar backscatter, the theorem of the central limits holds to represent the stochastic properties of the phase (complex random Gaussian circular variable). Analytical expressions can be derived for the phase standard deviation for different multilook factors [*Curlander and McDonough*, 1991; *Just and Bamler*, 1994; *Lee et al.*, 1994; *Hanssen*, 2001]. However, if the multilook factor (or number of independent looks, L) is large, an empirical expression can be used [*Rodriguez and Martin*, 1992], which asymptotically approaches the analytical solution (for $L > 4$):

$$\sigma_{\varphi}^{2}(\rho) = \frac{1}{2L}\frac{1-\rho^{2}}{\rho^{2}}. \quad (1)$$

In that way, we can estimate the differential phase variance (σ_{φ}^{2}) due to decorrelation as a function of the coherence value (ρ). Equation (1) can be expressed as LOS range change:

$$\sigma_{\varphi}^{2}(\rho) = \frac{\lambda}{4\pi}\frac{1-\rho^{2}}{2\rho^{2}}, \quad (2)$$

where λ is the SAR wavelength.

2.2. Geometric Residuals: Orbital and Topography

[11] Typically, orbital ephemerides are not accurate enough to correctly model baseline parameters. Uncertainties in the order of ±7 and ±30 cm in azimuth and range directions have been reported [*Scharroo and Visser*, 1998]. Thus, assuming that orbital path errors are correlated and vary slowly with azimuth/acquisition time (~15 sec. for standard frame of ERS-like SAR sensor), the orbital uncertainties would generate smooth trends. To correct orbital effects, several methods have been proposed [*Massonnet and Feigl*, 1998; *Biggs et al.*, 2007]. However, after unwrapping, a low order polynomial model is suitable to remove them [*Hanssen*, 2001]. We found that typically solving for a biquadratic model parameters is enough to reduce significantly this effect, in the following we assume that for wavelengths (<half-width of the SAR image footprint), the residual shorter spatial errors are spatially uncorrelated ($\sigma_{\varphi_{orb-corr}}^{2}$).

[12] Residual topographic errors remain after topography subtraction due to (1) used DEM inaccuracy, or (2) actual vertical shifts between target height and nearby DEM posting values. The first effect could propagate to the differential phase and add as random phase noise according to, $\sigma_{\varphi_h}^{2} = \left(\frac{4\pi B_{\perp}}{\lambda R \sin\theta}\right)^{2}\sigma_{h}^{2}$, where $B_{\perp}$ is perpendicular baseline, R is the slant-range distance, θ is the local incidence angle and σ_{h}^{2} is the DEM height variance. However, using small baselines would diminish this effect with respect to other error sources. Its stochastic properties can generally be assumed spatially random, except for DEM in urban areas or digitized topographic maps where considerable spatial correlation can occur. However, the later scales with the perpendicular baseline and can be estimated during the model inversion.

2.3. Atmospheric: Ionosphere and Troposphere

[13] The ultimate limiting factor for geodetic radio-based techniques is propagation delay through the atmosphere [*Blewitt*, 2007]. Geodetically, the atmosphere can be divided into two simple layers, ionosphere (conductive atmosphere, 50–2500 km height) and troposphere (neutral atmosphere, <20−50 km).

[14] The delay is a function of the refraction index (n). The ionosphere behaves as a dispersive media ($n < 1$), so induces a delay in the group velocity [*Hofmann-Wellenhof et al.*, 2007]. In particular, ionospheric refraction index depends on electronic density and inversely on the square signal frequency. However, normally the spatial distribution (horizontal gradient) of the ionospheric refraction index is relatively homogeneous at the SAR image scales (~100 km) [*Bürgmann et al.*, 2000]. Moreover, large spatial gradients can be significant at equatorial and polar regions. So, low order polynomial models could easily remove such effects and the residual can be again considered spatially uncorrelated. It is worth noting that, for longer SAR wavelengths, the ionospheric delays can be pronounced [*Meyer et al.*, 2006].

[15] Yet the neutral atmosphere (troposphere) is by far the largest error source in DInSAR [*Goldstein*, 1995; *Zebker et al.*, 1997]. The radar delay in the troposphere is caused by spatial and temporal changes in water vapor, pressure, and/or temperature, which changes the refractivity index [*Hanssen*, 2001; *Puysségur et al.*, 2007]. There are two clear components that affect the tropospheric radar delay (dry and wet). These effects correlate well with two different atmospheric processes: (1) the dependence on height of the temperature and pressure, and (2) the water content motion and mixing which is larger at low elevations (due to higher temperatures) [*Hanssen*, 2001].

2.3.1. Vertical Stratification

[16] Changes in the pressure and temperature vertical profiles lead to changes in the hydrostatic equilibrium of dry atmospheric gases, producing a hydrostatic radar delay [*Hanssen*, 1998]. The hydrostatic delay (2.1 m) can be predicted at the millimeter scale using meteorological data [*Bevis et al.*, 1992] and using well established vertical static models [*Saastamoinen*, 1972]. When pressure and temperature profiles change with time, the total hydrostatic delay varies. However, only if local topography is prominent with respect to the vertical hydrostatic delay gradients, those delays could cause a differential phase contribution. Among several correction methods [*Delacourt et al.*, 1998; *Bonforte et al.*, 2002; *Wadge et al.*, 2002; *Li et al.*, 2005, 2006; *Onn and Zebker*, 2006; *Foster et al.*, 2006; *Puysségur et al.*, 2007], the use of an elevation-dependent polynomial model seems a very effective tool in most cases [*Cavaliè et al.*, 2007; *Elliott et al.*, 2008; *Doin et al.*, 2009]. Here, after application of the elevation-dependent polynomial model the corrected differential phase is assumed uncorrelated to this effect ($\varphi_{corr-topo} = \varphi - \varphi_{topo-dep}$).

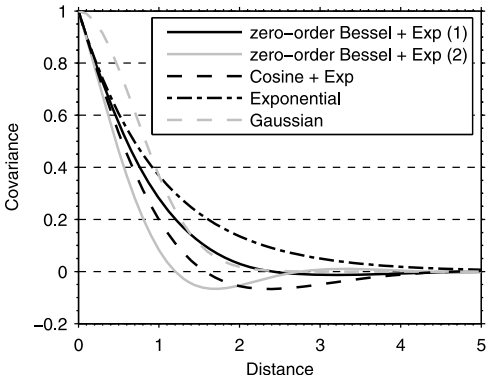

Figure 2. Theoretical covariance models [*Isaaks and Srivastava*, 1989]. Parameter b at zero-order Bessel + exponential function take value of 1 and 2 to illustrate its flexibility to account for the hole effect. Other model parameters are set to unity in the cosine + exponential, exponential and gaussian covariance functions.

2.3.2. Turbulence Mixing

[17] Changes in pressure, temperature and water vapor are larger below the planetary boundary layer (<1–4 km). In the lower troposphere, water vapor is the largest source of changes in the refraction index and consequently in the radar delay [*Zebker et al.*, 1997; *Williams et al.*, 1998]. The water vapor is transported and redistributed both vertically and horizontally by both, local and large-scale atmospheric circulation. The atmospheric circulation is governed by low Reynolds number fluid dynamics, and such fluid flow causes turbulences [*Tatarski*, 1961], which are reflected in the spatial and temporal fractal water vapor distribution [*Hanssen et al.*, 1999; *Hanssen*, 2001].

[18] High non-linear turbulent fluid flows are difficult to model in a deterministic way [*Middleton and Wilcock*, 1994]. Commonly, such flows are described from a stochastic approach, describing their statistical properties. Stochastic modeling can be performed using well-known tools, such spectral analysis, fractal analysis, geostatistics, etc. Using frequently used assumptions (stationary isotropic random process), the turbulent water vapor delay can be described with the covariance function:

$$C_{\varphi\varphi}(r) = \frac{1}{m}\sum_{i=1}^{m} \varphi(\underline{x}_i)\cdot\varphi(\underline{x}_i + r), \tag{3}$$

which only depends on distance (r) and m is the number of data points separated by a certain range of r. Atmospheric gravity waves are a clear exception to these assumptions [*Lyons and Sandwell*, 2003, and references therein], that recently have been modeled [*Knospe and Jonsson*, 2010]. However, most of the interferograms show more homogeneous atmospheric delay structures. Empirical covariance functions can be computed from the autocorrelation function or interferogram power spectra indirectly, or directly from a large sample of randomly selected points. The empirical covariance functions can be fitted to theoretical covariance functions to construct the covariance matrix that define the tropospheric turbulent phase errors. There are a large number of theoretical covariance models, some of which are shown in Figure 2. We selected the zero-order Bessel + exponential function [*Barzaghi and Sansò*, 1983]:

$$C_{\varphi\varphi}(r) = aJ_o(br)e^{-cr}, \tag{4}$$

where a, b and c are model parameters that control the initial amplitude, the damping effect of the bessel function and the exponential decay, respectively. This model can take into account the hole effect (anticorrelation) commonly observed in interferograms. The cosine + exponential function ($C_{\varphi\varphi}(r) = a\, e^{-r/b}\cos(r/c)$) can also model the hole effect [*Sudhaus and Jonsson*, 2009], but it can be numerically unstable, if the parameter c tends to zero. We can easily determine the variance-covariance matrix $\Sigma_{\varphi\varphi}$, using the fitted parameters of the theoretical covariance function [*González et al.*, 2010].

2.4. Unwrapping

[19] Phase unwrapping errors are particularly problematic. In general, phase unwrapping is an ill-posed problem and is non-trivial in the presence of decorrelation areas and phase noise [*Massonnet and Feigl*, 1998; *Hanssen*, 2001]. *Usai* [2003] proposed a method based on closed-loop conditions, following that

$$\varphi^{t_1t_2} + \varphi^{t_3t_1} + \varphi^{t_2t_3} = 0, \tag{5}$$

for the case of 3 interferograms. This method is not limited to such triangular configuration (loops around 4 interferograms or more can be done). However, the method is extremely elaborated and has not been used often [*Biggs et al.*, 2007]. So, we will assume that phase unwrapping will not contribute significantly to the phase, because poor quality interferograms will be rejected.

3. Ground Displacement Error Estimation in Multitemporal SB Method

[20] We choose the basic SB approach because our target regions are volcanoes and/or fault systems commonly located in non-urban areas. SB minimizes baseline decorrelation and topographic residuals (short spatial baselines), and also reduces the temporal correlation through a multilooking process. The SB multitemporal interferometric model has been extended with a rigorous Gauss-Markov mathematical model (a common geodetic data analysis model - observations adjustment and hypothesis testing). The model is used to rigorously establish observations and problem unknown uncertainties. The model is composed of a functional or deterministic model used to characterize the physical or geometrical problem relationships between observations and unknowns and a stochastic model useful for describing the stochastic properties of observations, unknowns and even their relationships [*Vanicek and Krakiwsky*, 1986; *Hanssen*, 2001; *Teunissen*, 2003].

3.1. Determinist or Functional Model

[21] We assume that the differential interferometric phase for the x-pixel in the k-interferogram is unwrapped ($\varphi^k_{x,unw}$),

and unwrapping is error-free. So, the phase can be represented as the sum of phase contributions:

$$\varphi^k_{x,unw} = \varphi^k_{x,topo} + \varphi^k_{x,defo} + \varphi^k_{x,atm} + \varphi^k_{x,orb} + \varphi^k_{x,\varepsilon}, \quad (6)$$

where $\varphi^k_{x,topo}$ is the residual topographic differential phase; $\varphi^k_{x,defo}$ is the differential phase due to displacement between acquisition times (i, j); $\varphi^k_{x,atm}$ is the differential phase due to relative atmospheric delay at acquisition times (i, j); $\varphi^k_{x,orb}$ relative phase contribution due to satellite orbits; and $\varphi^k_{x,\varepsilon}$ are other error contributions due to processing, decorrelation, etc.

[22] The model presented in (6) relating an observation ($\varphi^k_{x,unw}$) with, at least, 5 unknown parameters ($\varphi^k_{x,topo}$, $\varphi^k_{x,defo}$, $\varphi^i_{x,atm}$, $\varphi^j_{x,atm}$, and $\varphi^k_{x,orb}$) is clearly rank-deficient and cannot be solved. The classical differential interferometric approach assumes that all contributions are negligible except some interest-parameter (deformation, topography or atmospheric delay). An alternative for overcoming the rank deficiency can be to remove/reduce parameters or combine observations ($\varphi^k_{x,unw}$, where $k \geq 5$). The latter leads to the alternative model known as advanced, stack, multibaselines and/or time series interferometric methods.

3.1.1. Unknown Parameters

[23] The SB multitemporal interferometric method deals basically with the estimation of terrain deformation evolution and residual topography. In our approach, other phase contributions in (6) have been properly removed with preprocessing (atmospheric stratification and orbital trends) or have been included into the stochastic model (atmospheric turbulent delay). So, the observed differential phase is related to the two unknown parameters, for the deformation:

$$\varphi^k_{x,defo} = -\frac{4\pi}{\lambda} \cdot \left(u^j_{x,los} - u^i_{x,los} \right) = -\frac{4\pi}{\lambda} \cdot \Delta u^k_{x,los}, \quad (7)$$

where $\Delta u^k_{x,los}$ is the displacement in *los* between two time acquisitions (i, j) forming in the interferogram, k. For the residual topography

$$\varphi^k_{x,topo} = -\frac{4\pi}{\lambda} \left(\frac{B^k_{\perp,x}}{R^i_x \sin \theta^i_x} \right) \cdot \Delta h_x, \quad (8)$$

where $B^k_{\perp,x}$ is the perpendicular baseline, R^i_x is the slant angle between antenna position and pixel x, and θ^i_x is the local incidence angle. Unlike with deformation, which varies with time, the residual topography (Δh_x) for each pixel would remain the same as long as we use the same DEM during the differential interferometric processing.

3.1.2. Problem Formulation

[24] Consider $n + 1$ SAR images over a study area, acquired in chronological order at epochs $t = [t_o, t_1, ..t_n]$. These images can be combined to form K interferograms. So, assuming that the unwrapped phase of each differential interferogram ($\varphi^k_{x,unw}$, with $k = 1, .., K$) is referred to a certain pixel (x_o) of stable deformation history, and to the first epoch for which the deformation of all pixels is zero ($\varphi^{to}_{x,unw} = 0, \forall x$). The K observations $\varphi^k_{x,unw}$ can be related to $N + 1$ unknown parameters ($\underline{x}$). So, for each pixel we can construct a linear model such as

$$A\underline{x} = \underline{\varphi}, \quad (9)$$

where $\underline{\varphi}$ is the observation vector of length K, A is a design matrix with dimensions $K \times N + 1$, and $\underline{x}$ is an unknown parameter vector, which contains the deformation in the N epochs and the residual topography. According to the rule of using the older SAR image as master, we have $\varphi^k_{x,unw} = \varphi^{t_j}_x - \varphi^{t_i}_x$, where $t_j > t_i$, therefore, the matrix A fills for each row (useful interferogram k) with -1 for master epoch (t_i) and 1 for the slave (t_j), and zeros for the remaining epochs. For the additional residual topography parameter we add the last column, resulting in a matrix of the following kind:

$$A = -\frac{4\pi}{\lambda} \begin{bmatrix} -1 & 1 & 0 & 0 & 0 & \cdots & \frac{B^{t1}_{\perp,x}}{R^t_x \sin \theta^t_x} \\ 0 & -1 & 1 & 0 & 0 & \cdots & \frac{B^{t2}_{\perp,x}}{R^t_x \sin \theta^t_x} \\ 0 & -1 & 0 & 0 & 1 & \cdots & \frac{B^{t3}_{\perp,x}}{R^t_x \sin \theta^t_x} \\ 0 & 0 & -1 & 1 & 0 & \cdots & \frac{B^{t4}_{\perp,x}}{R^t_x \sin \theta^t_x} \\ 0 & 0 & 0 & -1 & 1 & \cdots & \frac{B^{t5}_{\perp,x}}{R^t_x \sin \theta^t_x} \\ \vdots & & \ddots & & & \vdots & \vdots \\ \cdots & & \cdots & & & \cdots & \frac{B^{tk}_{\perp,x}}{R^t_x \sin \theta^t_x} \end{bmatrix}. \quad (10)$$

[25] As previously seen, if we assume that observations contains errors, this model becomes

$$A\underline{x} - \underline{\varphi} = \underline{v}, \quad (11)$$

where $\underline{v}$ is the residual vector of length K. For subsequent treatment in the least squares formalism, we assume that errors are normally distributed and $E\{\underline{v}\} = 0$. If we have used all SAR images to form interconnected interferograms, the rank of $A \geq N + 1$, and the system is compatible [*Teunissen*, 2003].

3.2. Stochastic Model

[26] Whereas the functional model relates observations with unknown parameters, the stochastic model characterizes the a priori precision of the observations through its variance-covariances matrix. This characterization directly affects the precision of the estimated unknown parameters of the functional model. So, the stochastic model is defined generically as [*Hanssen*, 2001]

$$\Sigma_{\varphi\varphi} = \sigma^2_o Q_{\varphi\varphi}, \quad (12)$$

where $Q_{\varphi\varphi}$ is the cofactor matrix of dimensions $K \times K$, and σ^2_o the a-priori variance factor of the unit weight, which is considered $\sigma^2_o = 1$.

3.2.1. Spatial Variance-Covariance Matrix (Intrainterferogram)

[27] For convenience, we divide the variance-covariance matrix of the observations ($\Sigma_{\varphi\varphi}$) into spatial and temporal matrices. As presented in section 2, each interferogram is affected by spatially correlated and uncorrelated errors:

$$\Sigma_{\varphi\varphi} = \Sigma_{\varphi_{decorr}} + \Sigma_{\varphi_{res-topo}} + \Sigma_{\varphi_{orb}} + \Sigma_{\varphi_{atm}}, \quad (13)$$

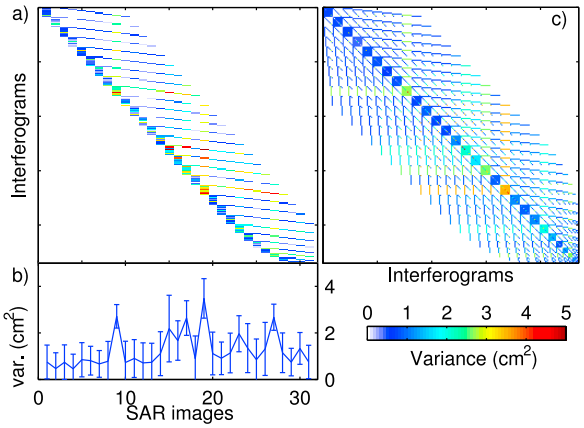

Figure 3. (a) Interferogram phase variances obtained as the estimated zero-lag covariance function value, at first instance, we attributed the same level of noise to both SAR images. (b) Estimated SAR image phase variance, those values compare well with the simulated atmospheric screen phases for each SAR image (Figure S3 of the auxiliary material). (c) Temporal interferometric phase variance-covariance matrix (equation (19)). All given units are in cm^2. The abbreviation var. stands for variance.

where the phase error components $\Sigma_{\varphi_{decorr}}$ and $\Sigma_{\varphi_{res-topo}}$ can be safely considered uncorrelated and $\Sigma_{\varphi_{orb}}$ as well, assuming correct inteferogram preprocessing. However, the atmospheric phase error ($\Sigma_{\varphi_{atm}}$) is clearly correlated in space. If we consider the spatial correlations, the full spatial variance-covariance matrix ($\Sigma^s_{\varphi\varphi}$) would have the form of a block diagonal matrix, as

$$\Sigma^s_{\varphi\varphi} = \begin{bmatrix} \Sigma^{k_1}_{\varphi\varphi} & 0 & 0 & \cdots & 0 \\ 0 & \Sigma^{k_2}_{\varphi\varphi} & 0 & \cdots & 0 \\ 0 & 0 & \Sigma^{k_3}_{\varphi\varphi} & 0 & \vdots \\ \vdots & \cdots & 0 & \ddots & 0 \\ 0 & \cdots & \cdots & 0 & \Sigma^{k_K}_{\varphi\varphi} \end{bmatrix}, \tag{14}$$

where each block corresponds to each interferogram variance-covariance matrix. Assuming, typical existing databases with dozens of SAR images from which hundreds of interferograms can be formed. This approach leads to vectors and matrices of enormous sizes which mean that resolving such problems remain challenging. Its solution will involve the use of optimized/recursive matrix algebra algorithms or subspaces solutions, that should be explored in the future.

[28] Consequently, we will maintain a typical pixel-by-pixel treatment that does not include the intrainterferogram spatial correlations. So, the spatial variance-covariance matrix of observations can be written as

$$\Sigma^s_{\varphi\varphi} = diag\left(\sigma^2_{decorr,k} + \sigma^2_{res-topo,k} + \sigma^2_{orb,k} + \sigma^2_{atm,k}\right), \tag{15}$$

where $diag(\cdot)$ represents the diagonal matrix of dimensions $K \times K$, whose main diagonal elements are the sum of phase variances, for $k = 1, .., K$.

3.2.2. Temporal Variance-Covariance Matrix (Interinterferogram)

[29] Considering K interferograms with temporal separation longer than a day ($t_j - t_i \geq 1$ day), phase observations can largely be assumed temporally uncorrelated [*Williams et al.*, 1998; *Hanssen*, 2001]. However, the multiple use of a specific SAR image to form several interferograms introduce an observation correlation, which can be taken into account in the parameter estimation [*Emardson et al.*, 2003]. So, equation (12) becomes the sum of two components: the spatial and temporal variance-covariance matrices:

$$\Sigma_{\varphi\varphi} = \Sigma^s_{\varphi\varphi} + \Sigma^{tmp}_{\varphi\varphi}, \tag{16}$$

where $\Sigma^{tmp}_{\varphi\varphi}$ accounts for temporal correlated terms (data redundancy).

[30] To account for data redundancy correlation, we assume the same rationale as *Emardson et al.* [2003]. Thus, if e.g. we have two interferograms ($K = 2, [\varphi^{t_1t_2}, \varphi^{t_2t_3}]$) formed by 3 time-separated SAR images ($t_1 < t_2 < t_3$), the variance of interferograms can be expressed as

$$\begin{aligned} \sigma^2_{\varphi^{t_1t_2}} &= \sigma^2_{\varphi^{t_1}} + \sigma^2_{\varphi^{t_2}} \\ \sigma^2_{\varphi^{t_2t_3}} &= \sigma^2_{\varphi^{t_2}} + \sigma^2_{\varphi^{t_3}} \end{aligned} \tag{17}$$

so, it is automatic that the only common factor is the common use of t_2. If we assume the covariance between both measurements ($\varphi^{t_1t_2}$, $\varphi^{t_2t_3}$) is

$$Cov(\varphi^{t_1t_2}, \varphi^{t_2t_3}) = \sigma^2_{\varphi^{t_2}}, \tag{18}$$

we can form the temporal variance-covariance, for this case, as

$$\Sigma^{tmp}_{\varphi\varphi} = \begin{bmatrix} \sigma^2_{\varphi^{t_1t_2}} & \sigma^2_{\varphi^{t_2}} \\ \sigma^2_{\varphi^{t_2}} & \sigma^2_{\varphi^{t_2t_3}} \end{bmatrix}. \tag{19}$$

[31] Therefore, to obtain the temporal correlations (covariances), we should estimate the phase error (variance) of each SAR image ($\sigma^2_{\varphi^{tm+1}}$). We propose to estimate it as the mean of the estimated variances of each interferogram (Figure 3a). The phase variance of each interferogram is obtained from a best-fitting covariance model at zero-lag (e.g., the proposed zero-order Bessel and exponential decay model). It assumes that the major common phase variance source is the turbulent atmospheric delay at each specific epoch. Once estimated, we can fill out the off-diagonal elements of the temporal variance-covariance matrix (Figure 3b), zeros elsewhere except for interferograms sharing a SAR image, where we introduce the estimate of SAR phase variance (equation (18)). In Figure 3, we illustrate this using actual data from the simulated SAR data set in section 4. This approach allows us to take into account the temporal distribution of a set of non-independent interferograms (SB-like methods).

[32] However, the SAR phase variance estimation method can only approximate the relative weight of each SAR image phase in a set of interferograms. Thus, we propose adding a Montecarlo resampling method to avoid biasing the estimated uncertainties. We use the bootstrap method, which

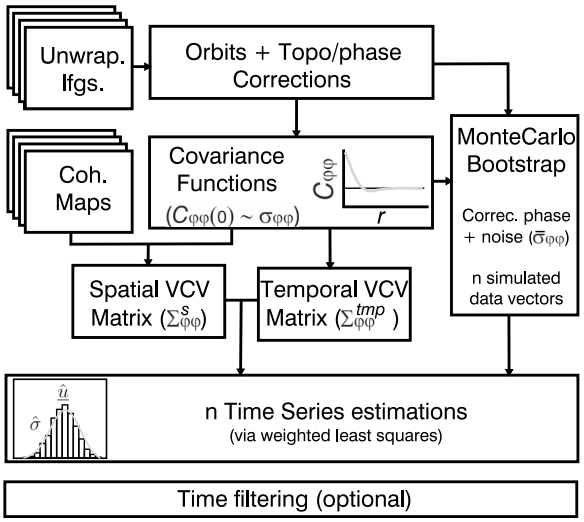

Figure 4. Schematic program flowchart of multitemporal InSAR processing with error estimation model (see text for details).

implies the perturbation of the observations with realistic noise simulations [*Efron*, 1979]. It iterates a sufficiently large number of times until a searched probability density function is well characterized. Our tests indicates that at least 100 samples should be carried out, with minor differences as increasing the number of iterations (<10% in the estimated standard deviations, for 1000 samples). We introduce the bootstrap method over the vector of observations instead of perturbing equation (16) to avoid likely non-positive definite matrices resulting in poorly conditioned and unstable solutions. To generate the noise, we impose a uniform probability density function with standard deviation as the mean of the standard deviations of all interferograms used as computed using the best-fitting covariance models.

3.3. Least Squares Solution

[33] For each bootstrapped observation vector ($\underline{\varphi}^*$), we solve the linear system of equations by means of the least squares method, which minimizes the following norm of the residuals, $\underline{v}^t P \underline{v}$ [*Teunissen*, 2003]; with the solution estimate:

$$\underline{\hat{x}} = (A^t P A)^{-1} A^t P \underline{\varphi}^*, \tag{20}$$

where $P = Q_{\varphi\varphi}^{-1}$ is the weighting matrix, and the estimated unknown parameters variance-covariance matrix is

$$\Sigma_{\underline{\hat{x}}\underline{\hat{x}}} = \sigma_o^2 (A^t P A)^{-1}. \tag{21}$$

[34] Finally, the global model test is applied to check if the problem is complete and consistent with the observations. It is also known as χ^2 test [*Usai*, 2003], and it compares the a-priori and posteriori variances, such as $\sigma_o^2 = \hat{\sigma}_o^2$ given a certain level of significance (typically 95%). However, other statistical hypothesis tests can also be applied [*Teunissen*, 2006].

[35] In Figure 4, we summarize the main steps in the proposed processing chain. Starting from unwrapped interferograms and their coherence maps, we correct each interferogram for possible trends (orbital or long-wavelength atmospheric, see sections 2.2 and 2.3) and for the phase-topography gradients (section 2.3.1). For each corrected interferogram, we compute its empirical covariance function and we obtain the estimated interferogram phase variance as the prediction of the best fitting covariance model at lag zero (section 2.3.2). Then, the compound variance-covariance (VCV) matrix is calculated (according to sections 3.2.1 and 3.2.2) as a sum of spatial and temporal matrices. Then, in a pixel-by-pixel basis, we simulate n times the vector of corrected interferogram phases using a bootstrap method using a uniform random probability density function with standard deviation, the mean of the estimated interferogram phase variances. We solve n times linear system of equations, and populate the posteriori marginal probability functions of the estimated deformation time series. Finally, time filtering might be applied.

4. Simulation Tests

[36] We used two sets of synthetic data to test the correct implementation and robustness of the proposed method. We simulated realistic conditions with temporal baseline distributions of SAR images similar to the ERS and ENVISAT European satellites. Simulations are progressively complex by adding different types of noise, due to atmospheric disturbances (spatially correlated noise) at the acquisition times and due to temporal decorrelation noise (white noise).

4.1. Linear Rate Test

[37] We started with a simple simulation with displacement constant rate and no errors. Three-dimensional displacement fields were simulated using a constant volume-change rate of -0.25×10^{-3} km^3/yr of an isotropic expansion center in an elastic half-space [*Mogi*, 1958] at a depth of 3.5 km (X: 5 km; Y: −5 km) for an area of 20 × 20 km^2. 3D displacements were simulated for 31 randomly selected epochs for a period of 9 years (1992–2001) and projected onto a descending orbit and $\theta = 23°$ (Figure S1 of the auxiliary material).[1] Then, we added a random atmospheric phase signal for each scene with the spectral power following a −5/3 for wavelength larger than 2 km and a spectral index of −8/3 for wavelength smaller than 2 km. Atmospheric phase signals were multiplied by a constant randomly selected between 0 and 4, to take into account the temporal variability of up to an order of magnitude of the atmospheric phase signals [*Hanssen*, 1998] (Figure S2 of the auxiliary material). We also added white noise (decorrelation and processing errors), with a standard deviation of 5 mm, which is equivalent to 30° for a SAR system with C-band wavelengths. Finally, simulated interferograms were obtained by differentiating the displacement fields at master and slave epochs. We generated all interferograms with a common selected temporal baseline constraint, $T < 4$ years, [*Fernández et al.*, 2009], leading to 234 simulated interferograms.

[38] In Figure 5, we show the results of the linear rate tests. Estimations were obtained applying the proposed method and a temporal Gaussian low-pass filter (width of 0.5 years). Figures 5a–5c show the linear velocity maps fitting a linear

[1] Auxiliary materials are available in the HTML. doi:10.1029/2011JB008412.

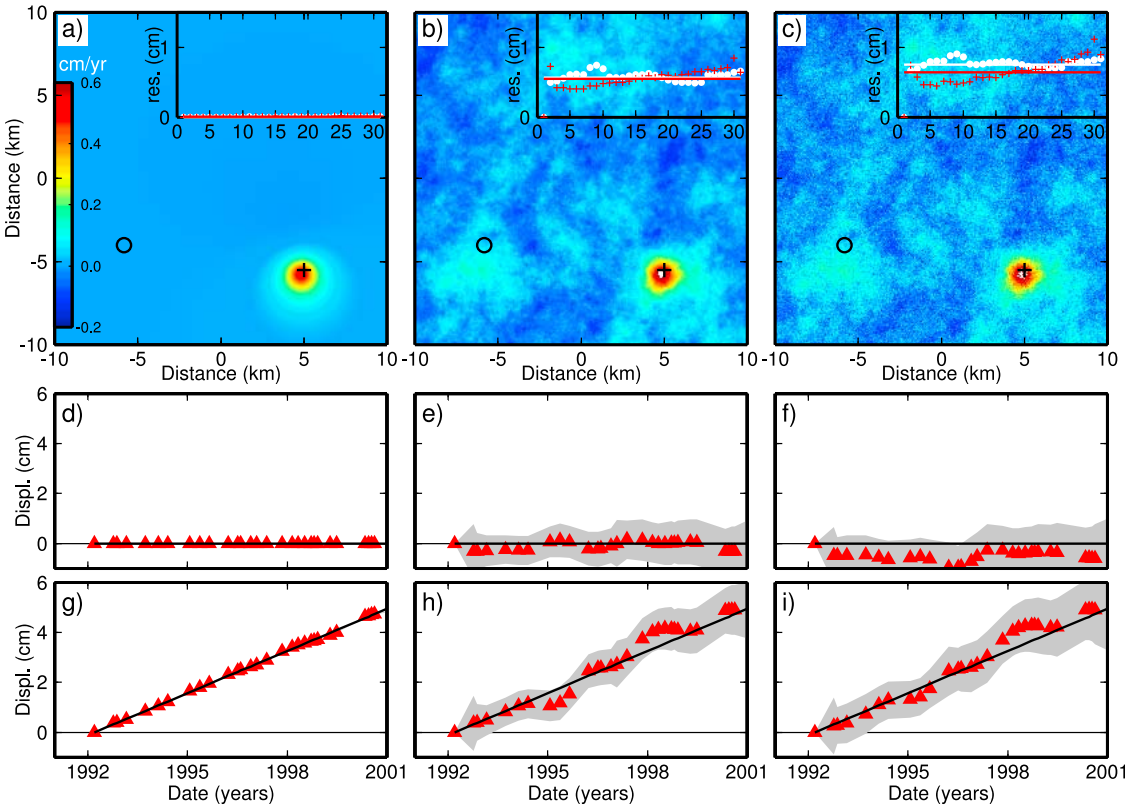

Figure 5. Synthetic linear temporal model tests: Fitted linear velocity maps of (a) the no noise simulation; (b) the atmospheric noise simulation; and (c) the atmospheric and decorrelation noise simulation (open circle, non-deforming point; cross, a deforming point). Insets in Figures 5a–5c illustrate, first the standard deviation of the residuals between the estimated and simulated time series (white points and its mean white line) and second the mean of the estimated standard deviations (red points and its mean red line). Time series results of the estimated displacements (red triangles) and bootstrap estimated 2-sigma uncertainties (gray area) and simulated (black line) for (d–f) a non-deforming point and (g–i) the maximum deforming point. Additional results in Figure S4 of the auxiliary material.

model to the time series of displacements for the three simulated scenarios (no noise; atmospheric; and atmospheric and decorrelation). Maps show consistent results with the increasing noise simulation. We show the estimated time series of displacements and the estimated errors of two points (Figures 5d–5i).

[39] In Figures 5d and 5g, the estimated time series of displacements and associated errors of the two points illustrate the example without noise. As expected, the disagreement is very small, and only slightly differences occur at the end of the time series in the case of the maximum deformation area. It is due to border effects of the temporal low-pass filter. We would point out that the estimated standard deviations computed using the bootstrap method are consistently small, based on the small mean and standard deviation of the calculated empirical variances. Figures 5e and 5h show the test case with atmospheric noise, and here the associated errors are much larger, but also the displacement estimations remain within the estimated errors. Finally, the last linear test case is shown in Figures 5f and 5i, where white noise errors were added. Also the estimated error bounds increase accordingly with the addition of the noise (~20% with respect to only atmospheric noise, in accordance with the increased simulated error). A significant result is that despite the magnitude of the signal, displacement estimations largely fall inside the estimated error bounds.

[40] In addition, we also checked the goodness of the error estimation by comparing the standard deviation of the residuals between the estimated displacement time series and the real simulated signal for each epoch and simulation test of all points (white data, inset graph in Figures 5a–5c), and the mean of the estimated standard deviations for all epochs and points (red data, inset graph in Figures 5a–5c). For the three linear simulation tests, the agreement is good. We also highlight that the largest differences are in the third scenario, with the actual residuals underestimated by about 10%.

4.2. Non-Linear Rate Test

[41] Here we simulated a more complex scenario with a nonlinear temporal displacement evolution using the following arbitrary expression (based on the vertical component of the Mogi model):

$$u = a\frac{-bt + ct^3}{(d^2 + 3.5r^2)^{3/2}}, \tag{22}$$

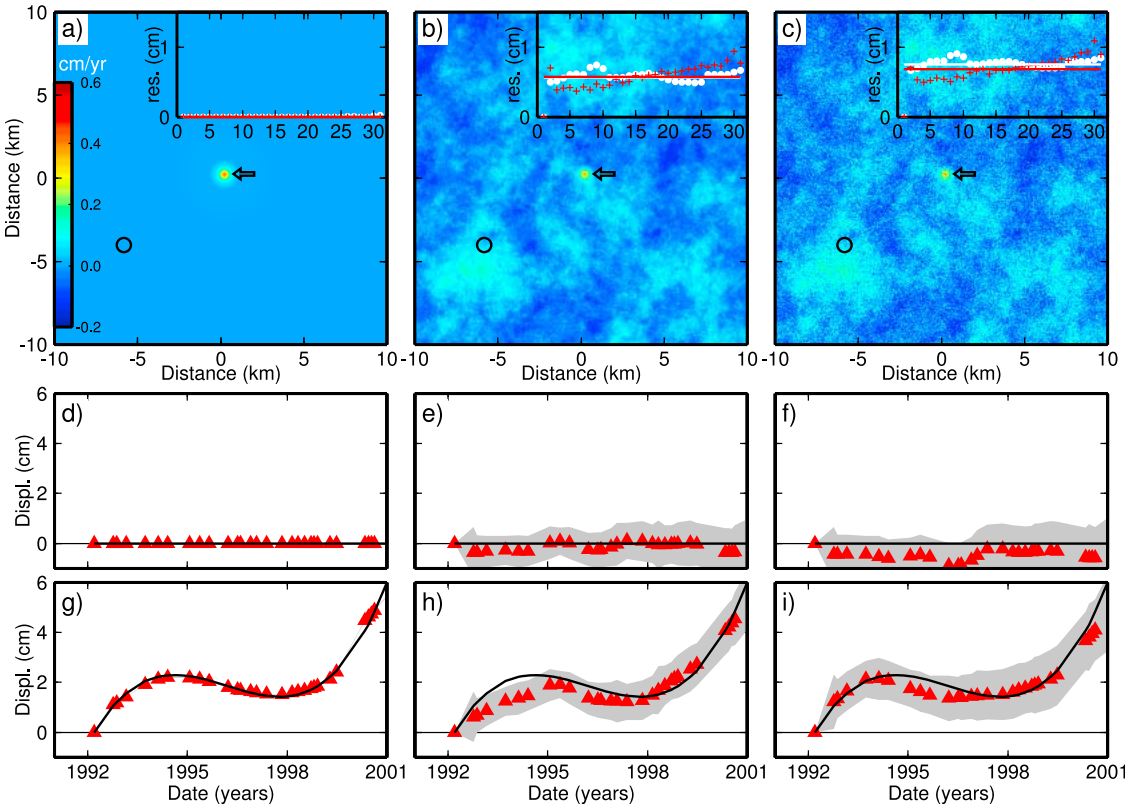

Figure 6. Synthetic non-linear temporal model tests: Fitted linear velocity maps of (a) the no noise simulation; (b) the atmospheric noise simulation; and c) the atmospheric and decorrelation noise simulation (open circle, non-deforming point; arrow, maximum deformation point). Insets in Figures 6a–6c illustrate, first the standard deviation of the residuals between the estimated and simulated time series (white points and its mean white line) and second the mean of the estimated standard deviations (red points and its mean red line). Time series results of the estimated displacements (red triangles) and bootstrap estimated 2-sigma uncertainties (gray area) and simulated (black line) for (d–f) a non-deforming point and (g–i) the maximum deforming point. Additional results in Figure S4. Used parameters were a = 100000, b = −0.015, c = 0.002, d = 1.5 km, and r = 0.25 km.

where u are displacements depending on time (t) with respect to the first epoch, a is a constant to modulate the displacement magnitude, b and c modify the displacement temporal evolution, d is a source depth parameter, and r is source radial distance (d and r change the displacement decay distance). The values used for these parameters are shown in the caption of Figure 6. This function allows us to simulate two periods of uplift ground displacement acceleration (in analogy with two volcanic unrest periods). The non-linear displacements were simulated at the same 31 epochs (1992–2001). As in the case of the linear displacements, three different simulations were performed using the same temporal combination of epochs (234 interferograms) and the same noise realization as in previous tests (atmospheric and decorrelation). However, in this case, we simulate the displacements affecting a relatively small area, smaller than the spatial scale of the atmospheric noise (Figures 6a–6c and Figure S3 of the auxiliary material).

[42] In Figure 6, we show the results of the non-linear rate tests. Estimations were obtained applying the proposed method and the same previous temporal filter. Figures 6a–6c show the non-linear velocity maps fitting a linear model to the time series of displacements for the three simulated scenarios (no noise; atmospheric; and atmospheric and decorrelation). Lower panels show the estimated time series of displacements and the estimated errors of two points (Figures 6d–6i). Figures 6d–6f show the results for a non-deforming region, while Figures 6g–6i show the results of the maximum deformation point (central point). In Figures 6d and 6g, results of the example without noise indicate good agreement. However, the effect of the temporal low-pass filter at the end of the time series tends to reduce them in all cases. The larger the deformation rates, the stronger this effect is (Figures 6g–6i). Figures 6e and 6h show results of the non-linear deformation with atmospheric noise, and the evolution of the displacements around 1994 is clearly underestimated. Finally, the displacement time series in the last simulation (non-linear deformation with atmospheric and decorrelation noise) remains clearly within the estimated errors bounds (2-sigma confidence interval).

[43] The goodness in the error estimation was checked as in the case of the linear simulation tests. The results of the

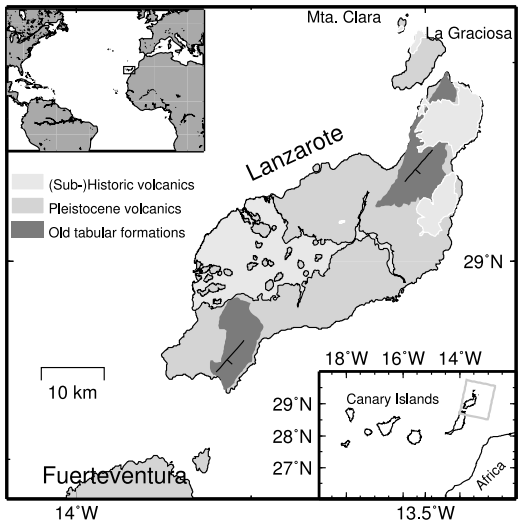

Figure 7. Geographic and sketch of the Lanzarote geology: 1) A tilted tabular basal formation, 2) Pleistocene volcanism and 3) the recent historic and sub-historic eruptive material (area with black contour indicates those erupted material during 1730–1736 eruption). Upper left inset indicates the location in the Atlantic Ocean. Lower right inset, the location in the Canary Islands archipelago (grey rectangle SAR images coverage).

non-linear case are also in agreement. We must point out that the testing results are based on the same error simulations, so it is not surprising that only small differences are present. It shows that the error estimation procedure is largely insensitive to the temporal behavior of the deformation signal and somewhat of the area affected (if the percentage of imaged area affected by deformation is small). We would also like to note that this approach is valid as long as the empirical covariance functions are not significantly biased by any other phase coherent signal (e.g., orbital ramps or large extension of signals), in that case the computation of the empirical covariance function can be constrained to a non-deforming area.

5. Application to Lanzarote Island

[44] This section presents the results from applying the new error estimation multitemporal method in Lanzarote Island (Figure 7). Lanzarote island is a volcanic oceanic island characterized by low volcanic activity and good conditions for interferometry [*Romero et al.*, 2003]. The Lanzarote Island hosted two of the 12 historic eruptions in the Canary Islands archipelago and in particular the 1730–1736 eruption, the longest (2055 days) and largest in volume of erupted material (~3 km^3, see caption Figure 7) in the last 500 years [*Araña and Ortíz*, 1991]. Eruptive activity is characterized by fissural eruptions of low-explosive basaltic magmas. Currently, superficial volcanic manifestation is limited to high temperature anomalies (around Montañas del Fuego, Timanfaya) [*Fernández et al.*, 1992]. Existing instrumentation (in particular, the Laboratorio de Geodinámica de Lanzarote, LGL, http://www.iag.csic.es/LGL/Index.html), has been used to study weak seismic signals (seismic swarms of low magnitude, <2), high heat flow and earth tide anomalies [*Arnoso et al.*, 2001; *Correig and Vila*, 1993; *Fernández et al.*, 1992]. More recently, *Romero et al.* [2003] analyzed a set of 6 ERS SAR images and showed the good conditions for interferometry (climate dry conditions and large extension of recent lava flows). They distinguished relatively important atmospheric contributions in the differential interferograms and no large ground deformations during the studied period (1992–2000). For this reason a multitemporal analysis of interferometric products and the assessment of the errors will be needed to resolve such small displacements.

5.1. Multitemporal Analysis

[45] Here, we used a set of 14 SAR scenes from the European Space Agency (ESA) of satellites ERS-1 and ERS-2, descending orbit (Table S1 of the auxiliary material), acquired in the period 1992–2000. We coregistered all scenes to a common master geometry (August 12, 1995), and further computed differential interferograms using the DORIS software [*Kampes et al.*, 2003]. We used a Shuttle Radar Topography Mission DEM to remove the topographic contribution. A spatial multilooking factor of 4 looks in range and 20 looks in azimuth produced pixel sizes on the ground of about 80 × 80 m. Due to the exceptionally good conditions for interferometry and a pre-selection of the SAR images (with small perpendicular baselines), we were able to make all possible interferogram combinations (91 differential interferograms, see Table S2 of the auxiliary material). In addition, we computed the coherence maps and the empirical covariance function for each interferogram (2500 data points were randomly selected to compute it).

[46] A subset of pixels (82619) was selected based on the average spatial coherence ($\overline{\rho} \geq 0.25$), thus reducing post-processing to ~20% of the total cropped pixels. Then, all unwrapped interferograms were analyzed using the proposed method to determine the spatial and temporal surface displacements. We took into account the phase variance depending on the decorrelation (equation (2)), phase variance due to turbulent troposphere (fitted zero-lag, equation (4)) and temporal distribution (redundancy) of the observations (equation (16)). To solve the problem, we fixed the deformation at the first epoch to zero. Finally, the inverted time series were filtered using a Gaussian low-pass filter with a window of 0.75 years, assuming that most of the atmospheric effects are uncorrelated with time.

6. Results

[47] In Figure 8a, we show the map of the linear velocity map from the estimated time series of displacements for each coherent pixel in mm/year. In addition, the mean square root of the residuals with respect to the linear model for all time series is of the order of ~±1 mm/year. First, most of the area of Lanzarote (and northern islets) is stable at the level of ~±1 mm/year during the studied period. Second, two areas (central part and northwestern coast) show significant lengthening displacement rates (most likely a subsidence signal). The largest deformation rates are associated to the Timanfaya eruption area (Montañas del Fuego) with linear

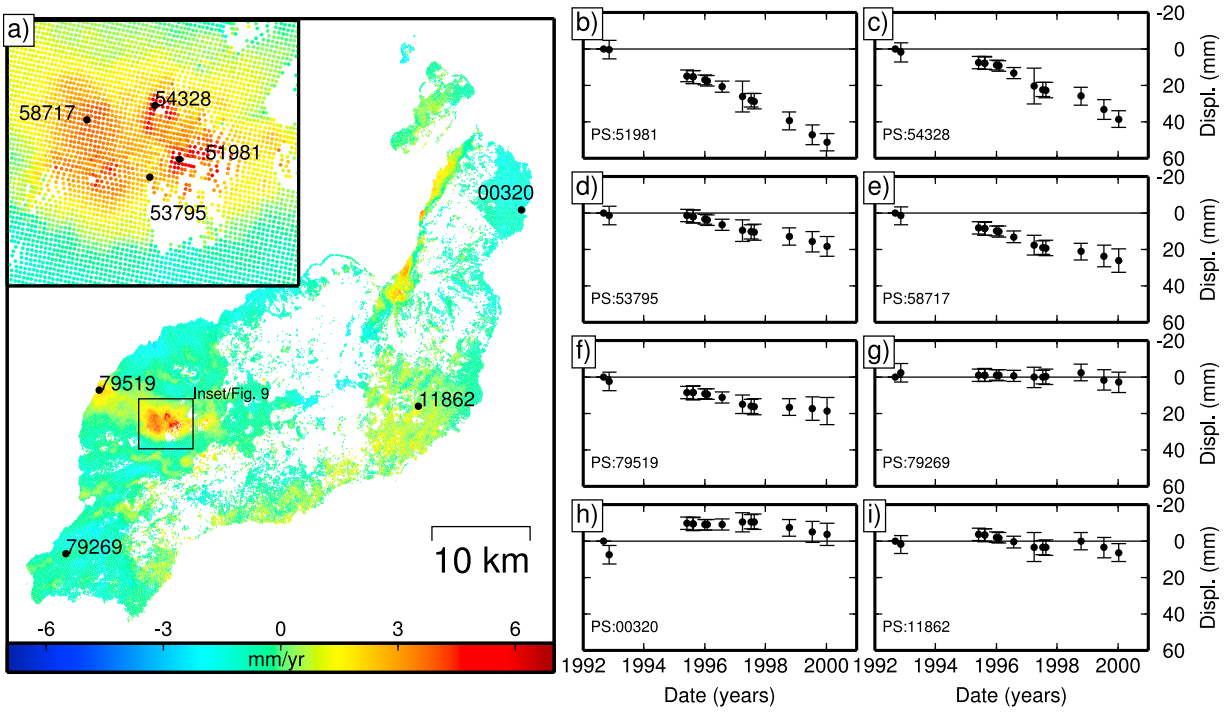

Figure 8. (a) Estimated descending linear deformation rate between 2 September 1992 to 8 January 2000. The black rectangle shows the location of Figure 9, as well the figure inset, which is a zoom into the Montañas del Fuego area (Timanfaya eruptive centers)). (b–i) Time series of displacements and associated estimated errors of 8 selected points. See text for details.

velocities of 4–6 mm/year, and affecting an area of ≈7 km^2. The second deformation area is smaller in magnitude (3–4 mm/year) and located on the northwestern coast. Despite the low magnitude of the deformation rate measured along the points between both deformation areas, points indicate systematic positive(subsidence) deformation rates. It could indicate spatial continuity and a possible connection between both areas (and the generating sources).

[48] In Figure 8a, we show the location of some selected time series (Figures 8b–8i). Time series represent the estimated displacement evolution and associated estimated error (displayed as 2-sigma error bars) for 8 coherent pixels. Figures 8b–8e show four time series of points around the Montañas del Fuego, Figure 8f shows a point in the northwestern coast deformation area and Figures 8g–8i three examples from non-deforming areas. Results around Timanfaya area show a complex spatial pattern of deformation (Figure 8a, inset). However, temporal evolution of displacements is rather monotonically linear in time. The maximum deformation areas is located west of the crater rim of the Timanfaya volcano (Figure 8b), where subsidence reached 5 ± 0.4 cm. In Figure 8c we show a point located at the Islote del Hilario (highest heat flux area, IH in Figure 9) showing a subsidence of 3.8 ± 0.5 cm. An additional point is selected close to the location of the Timanfaya module of the LGL with ~2 cm of displacement (Figure 8d), but only significantly deformed after the middle of 1995. The last selected point (Figure 8e) shows more than 2 cm of subsidence, a point located in an area of high density of hornitos from the 1730–1736 eruption [*Carracedo et al.*, 1990]. An example of time series from the northwestern deformation area is shown in Figure 8f. The displacements are linear with time with accumulated displacement 1.8 ± 0.7 cm, together with an increase of the estimated errors. Finally, we show three time series of non-deforming areas (Figures 8g–8i), in particular the time series shown in Figure 8h corresponds to a point close to the Cueva de los Verdes and Jameos del Agua modules of LGL. These time series illustrate that the estimated errors are in the range of 5–8 mm, although the repeatability is slightly higher (~1 cm). This observation is in accordance with previous results about the reliability of SB techniques [*Casu et al.*, 2006]. Unfortunately, for the Lanzarote test case no independent ground deformation estimates are available to us. However, we also provide briefly another example of SAR data set processed with the presented technique, where we report the comparison with independent GPS data, corroborating the validity of the technique under the aforementioned assumptions (see Appendix A).

6.1. Interpretation

[49] The complex spatial pattern of deformation detected in the Montañas del Fuego area is composed by an E-W trending subsidence signal and two elongated roughly parallel NW-SE subsidence signals (Figures 8a and 9). Maximum deformation rates are located at Islote del Hilario (IH) and Hoya de los Camelleros-Timanfaya crater rim (HC), in Figure 9, both along the easternmost NW-SE trending subsidence signal. The first (IH) is located at the area of highest-

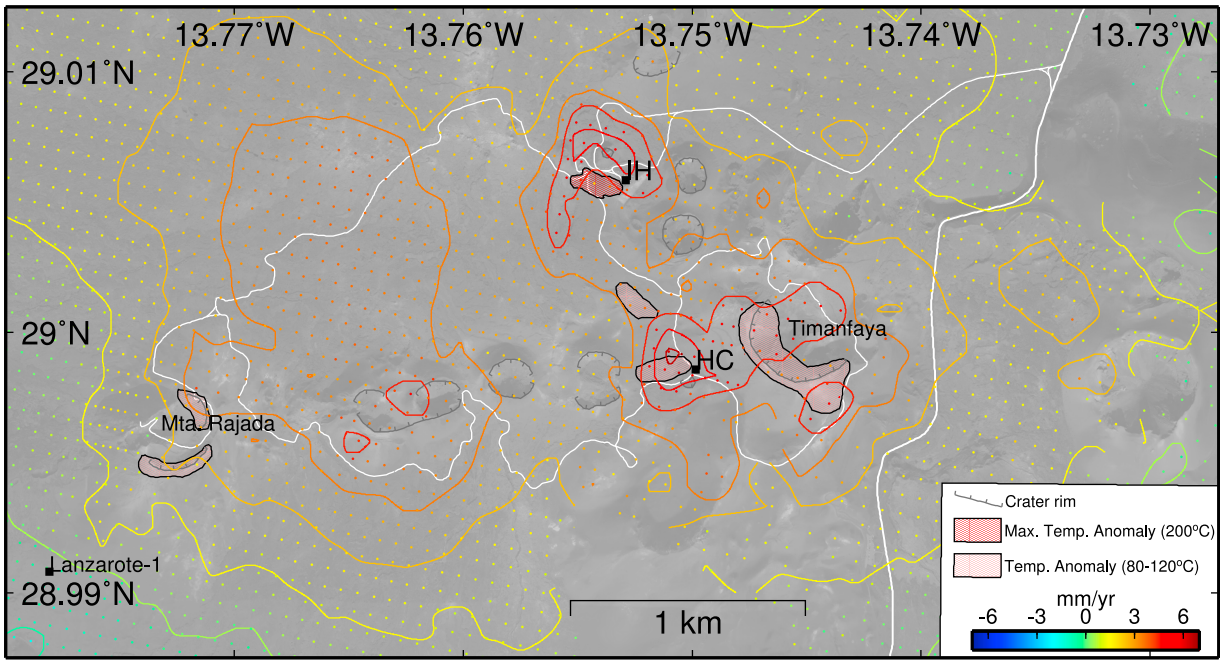

Figure 9. Interpolated and contoured linear velocity deformation (in mm/yr) over a local orthophoto of the Montañas del Fuego area (approximate location of the inset in Figure 8a). Red closed polygons mark high heat flux and anomalous temperature areas according to *Araña et al.* [1984]. IH and HC are indicating the Islote de Hilario and Hoya de los Camelleros, where maximum temperature anomalies are located. Lanzarote-1 marks the approximated location of a 2700 m deep geothermal exploration borehole. Mta. Rajada and Timanfaya are the major independent volcanic centers. White lines indicate asphalt paving roads.

heat flux and superficial temperature and the second area (HC) is located at the intersection of the easternmost NW-SE and E-W trending signals.

[50] The ground deformation location of the three preferentially directed signals seems to closely follow the structural pattern of the 1730–1736 eruptive fissures and emission centers [*Carracedo et al.*, 1990], and spatially coincides with the focused vertical conduit beneath Timanfaya volcano center (the longest-lived emission center of the 14-km long eruptive system), in the proximity of HC (Figure 9). In addition, the current spatial pattern of measured surface temperature anomalies (with up to ≈600°C at 13 m depth) reflects a volcanic origin, either due to magmatic processes (cooling and crystallization of a molten remnant in the 1730–1736 magmatic reservoir), a shallow hydrothermal-controlled fluid circulation, compaction of lavas or thermal-controlled deformation of a highly fractured media.

[51] To validate some of those hypothesis would require additional information and numerical models. In particular, we can discard the compaction of lavas because even in the case of thick lava flow accumulations can occur, the age and the fact that some deformation occur outside lava flows suggest that it is unlikely. So, our preferred solution is the existence of a long-lived thermally contracting shallow magma reservoir. It is also based on geophysical studies, which have inferred the presence of a partly molten magmatic chamber underneath Timanfaya area, at a depth of around 4 km [*Araña et al.*, 1984; *Fernández et al.*, 1992; *Camacho et al.*, 2001]. An additional constraint is the ~2700 m deep Lanzarote-1 borehole stratigraphy succession (Figure 9), where thickness of the volcanic material were determined to around 2400 meters. So, we speculate that the magmatic chamber might be located in or at the top of the sedimentary lid succession, where a magma negative buoyancy limit should be located and magma stagnation could be focused. Those depth ranges could explain the area affected by the deformation, because assuming a point source in an isotropic media (thermoelastic, elastic, ..), the radial distance affected by the deformation scales with the source depth. However, a model able to simulate the detected ground deformation and the presence of a high heat flow and temperature anomalies would require a more detailed analysis in the future.

7. Conclusions

[52] A novel method for the estimation of errors in multitemporal interferometric techniques (in particular, SB) has been presented. The method analyzes and quantifies the error contributions in each interferogram to invert the interferograms and obtain the displacement time series, following an appropriate weighting scheme. In addition a Monte Carlo method (bootstrapping) is used to improve the estimation of realistic error bounds in the unknown parameters (time displacement evolution). The simulation tests presented in section 4 confirm the goodness of the method and its

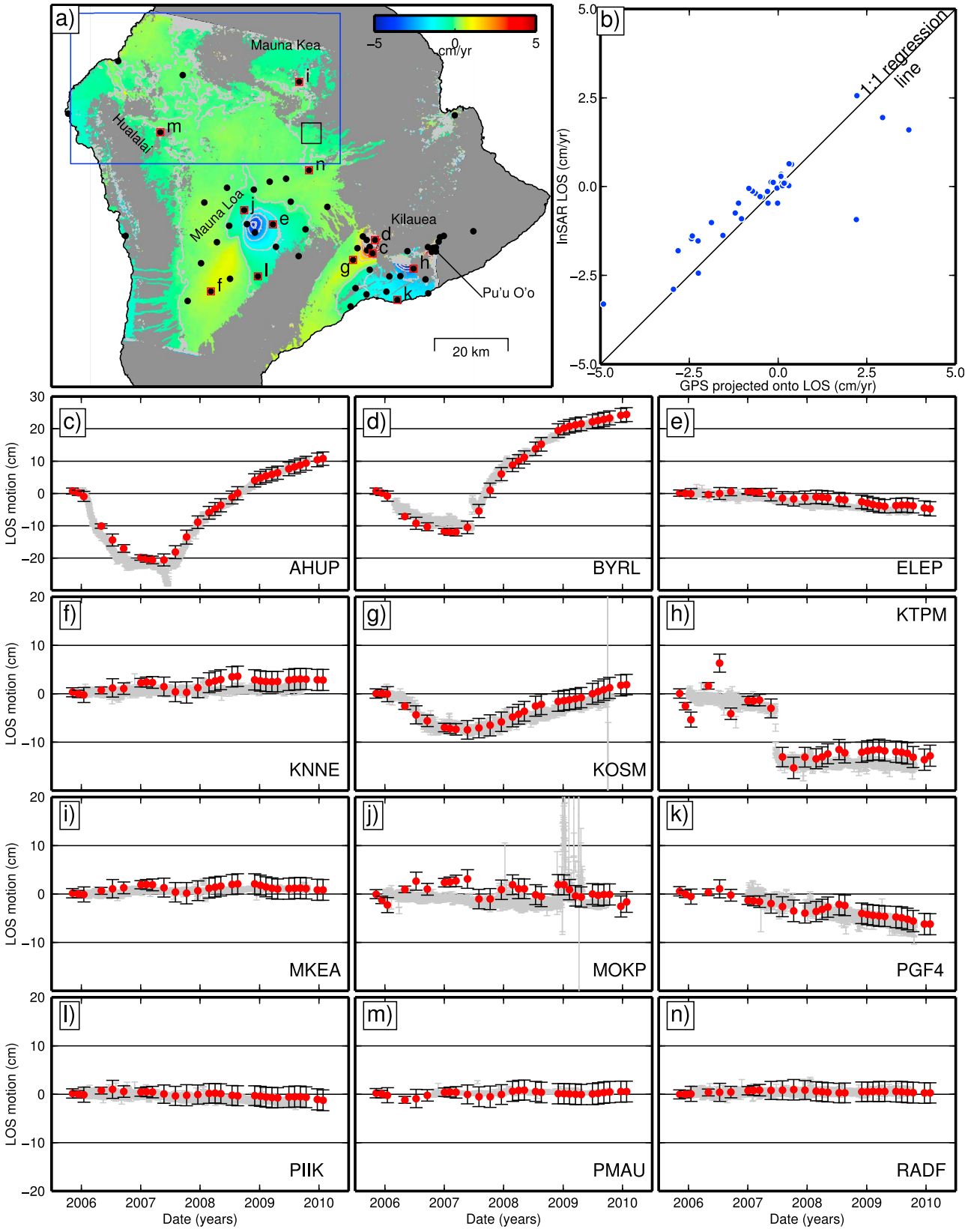
a)
Mauna Kea
Hualalai
Mauna Loa
Kilauea
Pu'u O'o
−5
0
5
cm/yr
20 km
b)
1:1 regression line
InSAR LOS (cm/yr)
GPS projected onto LOS (cm/yr)
c) AHUP
d) BYRL
e) ELEP
f) KNNE
g) KOSM
h) KTPM
i) MKEA
j) MOKP
k) PGF4
l) PIIK
m) PMAU
n) RADF
LOS motion (cm)
Date (years)
2006
2007
2008
2009
2010

Figure A1

correct implementation. The main advantage of the proposed method is to provide more realistic error assessment than previous techniques.

[53] The algorithm was applied to Lanzarote Island, for an interval period in which no magmatic activity occurred, and a time series for the displacement field and its uncertainty was retrieved. We detected deformation around Timanfaya volcano (Montañas del Fuego), where the last major eruption occurred (300 years ago). The deformation is consistent in time and indicates lengthening of distance to the satellite (a likely subsidence). The displacement field very closely follows the eruptive fissure pattern of the 1730–1736 eruption (the main E-W and a secondary NW-SE structural direction). The spatial extent of surface high temperature and high heat flux areas also support a generating process related with the magma crystallization (cooling and contraction) of the partly molten 300 year-old shallow (2–4 km depth) magmatic body under Timanfaya volcano, that fed the 1730–1736 eruption.

Appendix A: Comparison With GPS Data

[54] In this appendix, we present briefly results in another test case obtained with the presented multitemporal analysis technique. It is done, because unfortunately, for the Lanzarote test case no ground deformation estimates are available to us. So, it is in place to make a comparison/validation between potential results in other areas where ground true data is available. For that, we have selected Envisat SAR data from a descending pass (track 200) over the Big Island of Hawaii (SAR data from http://supersites.earthobservations.org/hawaii.php). At Hawaii, we have obtained daily GPS time series of some stations between 2006 to 2010 processed using a local reference frame approach [*Palano et al.*, 2010]. GPS stations estimates provide us with continuous three-dimensional measurements of the ground deformation, whereas the multitemporal analysis results give dense spatial maps of one-dimensional information for coherent areas. Both data sets allow for comparison of time series of surface ground deformation and their uncertainties (Figure A1).

[55] In Figure A1, we show the MTInSAR linear velocity estimated and the location of available GPS stations. Although, misleading due to temporal changing behavior of the volcanic sources, the obtained linear deformation field for the studied period is characterized by prominent signals of shortening of LOS (uplift) at Mauna Loa summit and LOS increase (subsidence) at Kilauea summit area (Figure A1a); subtle signals of subsidence on both volcanoes Southwestern rift zones (Figure A1b); Motion toward satellite in the Southern flank of Kilauea volcano (Figure A1c), and subsidence above the East Rift Zone. The deformation field shows no LOS ground motions in the Northern flank areas of Mauna Loa, and Mauna Kea and Hualalai volcanoes (Figure A1d).

[56] In Figure A1b, we correlate the linear velocity of the individual pixels (closest to the GPS stations) and compare with the best-fitting linear velocity model adjusted to the GPS time series data projected onto the satellite LOS direction to Envisat descending track. A linear correlation is obtained, however data scatters, indicating that results do not fully agree. It contrasts with previous comparison between both techniques (GPS-InSAR), a partial explanation is that due to the large displacements and the highly nonlinear ground deformation evolution a comparison between linear velocities will disagree in a larger amount, than comparison with low magnitude and steady state behavior test cases (as well avoidable unwrapping errors). In addition, another problem is that not all GPS stations cover the same period so it can bias the linear velocity estimation. Therefore, it is convenient to show a representative sample of the agreement between time series at individual sites (Figures A1c–A1n). Because MTInSAR results are relative measurements of displacements, we consider a stable reference area for comparison with respect to GPS, where nearby GPS stations also show minor displacement trends (we selected the black rectangle area in Figure A1a). Then, we assume zero deformation at the beginning of analyzed period 2006–2010. It was done by averaging the 10 initial daily solutions, when GPS data do not extend to the initial observation period a extrapolation of the first available epochs were performed, if not stable trends were present zero deformation was assumed at the time of the initial available epoch. Performing, these adjustment the agreement in the vast majority of the stations was obtained. It is particularly remarkable that even when the magnitude of displacement estimated by MTInSAR deviates with respect to the GPS one, the estimated 1-σ standard deviations indicate fairly good statistical agreement.

[57] Hawaii test case helps to further shown the potentials and limitations of the presented technique (assumptions and unsolved problems). It is particularly severe for areas northward or on the Eastern part the Kilauea East Rift Zone, which will require special attention during phase unwrapping prior to carry out the presented analysis. Those coherent areas are quite isolated and affected by intense ground deformation related to the Father's Day Intrusion episode (19–21 June 2007) and the vigorous activity of the lava lake at Pu'u'O'o vent. Therefore, results exhibit poor correlation with respect to near GPS station estimates (not shown here). It is noteworthy that the unwrapping process require future developments of the technique to account for or mitigate it.

Figure A1. (a) Mean LOS deformation velocity map overlaying a shaded DEM of Hawaii (in cm/yr, also contoured with gray lines at each cm/yr). Small black circles mark GPS stations sites (letters indicate stations displayed in Figures A1c–A1n). Blue rectangle is the area used to estimate orbital trends, topographic phase gradients and turbulent tropospheric effects. Labels indicate major volcanoes and the Pu'u O'o vent locations. (b) InSAR LOS velocities versus project GPS LOS velocities comparison for a point close to each station. Line 1:1 agreement is shown in black. (c–n) Comparisons of time series of displacement in cm for the analyzed period (2006–2010). MTInSAR ENVISAT results are represented as red dots with 1-σ estimated standard deviations black error bars. GPS project displacement time series and the propagated LOS uncertainties (error bars) are marked in gray.

[58] **Acknowledgments.** We are grateful to J.J. Mallorquí, G. Rodríguez-Velasco, J. Montero, and D. Carrasco for review of early draft. We also indebted to J.L.G. Pallero for insightful discussions about the method, David Hasting for the English review, and also Mimmo Palano for providing us the Hawaii GPS processed data (data courtesy of HVO and Stanford University). Comments by the Editor (T. Parsons), Associated Editor, and two anonymous reviewers helped us to improve the quality of the manuscript. Our research was supported by the Spanish MICINN projects: CGL2005-05500-C02, PCI2006-A7-0660, CGL2008-06426-C01-01/BTE, and AYA2010-17448. P.J.G. was partly supported by a UCM predoctoral fellowship, Ontario Early Researcher Award, NSERC-Aon Benfield/ICLR IRC. Data were kindly provided by ESA through DECIDE Volcano; ALOS/ADENAO3690 projects and Supersites Initiative. GMT software and MATLAB were used to create the figures. This work has been done in the frame of the Moncloa Campus of International Excellence (UCM-UPM, CSIC).

References

Amelung, F., S. Jónsson, H. Zebker, and P. Segall (2000), Widespread uplift and Trap-door faulting on Galápagos volcanoes observed with radar interferometry, *Nature*, *407*, 993–996, doi:10.1038/35039604.

Amelung, F., S. Yun, T. Walter, P. Segall, and S.-W. Kim (2007), Stress control of deep rift intrusion at Mauna Loa volcano, Hawaii, *Science*, *316*, 1026–1030, doi:10.1126/science.1140035.

Andersohn, J., M. Motagh, T. R. Walter, M. Roseneau, H. Kaufmann, and O. Oncken (2009), Surface deformation time series and source modeling for a volcanic complex system based on satellite wide swath and image mode interferometry: The Lazufre system, central Andes, *Remote Sens. Environ.*, *113*(10), 2062–2075, doi:10.1016/j.rse.2009.05.004.

Araña, V., and R. Ortíz (1991), The Canary Islands: Tectonics, magmatism and geodynamic framework, in *Magmatism in Extensional Structural Settings: The Phanerozoic African Plate*, edited by A. B. Kampunzu and R. T. Lubala, pp. 209–249, Springer, Berlin.

Araña, V., J. Díez, R. Ortíz, and J. Yuguero (1984), Convection of geothermal fluids in the Timanfaya volcanic area (Lanzarote, Canary Islands), *Bull. Volcanol.*, *47*(3), 667–677, doi:10.1007/BF01961234.

Arnoso, J., J. Fernández, and R. Vieira (2001), Interpretation of tidal gravity anomalies in Lanzarote, Canary Islands, *J. Geodyn.*, *31*, 341–354, doi:10.1016/S0264-3707(01)00003-5.

Barzaghi, R., and F. Sansò (1983), Sulla stima empirica della funzione di covarianza, *Boll. Geod. Sci. Affini*, *42*(7), 389–415.

Berardino, P., G. Fornaro, R. Lanari, and E. Sansosti (2002), A new algorithm for surface deformation monitoring based on small baseline differential SAR interferograms, *IEEE Trans. Geosci. Remote Sens.*, *40*(11), 2375–2383, doi:10.1109/TGRS.2002.803792.

Bevis, M., S. Businger, T. Herring, C. Rocken, R. Anthes, and R. Ware (1992), GPS meteorology: Remote sensing of atmospheric water vapor using the Global Positioning System, *J. Geophys. Res.*, *97*, 15,787–15,801, doi:1029/92JD01517.

Biggs, J., T. Wright, Z. Lu, and B. Parsons (2007), Multi-interferogram method for measuring interseismic deformation: Denali Fault, Alaska, *Geophys. J. Int.*, *170*, 1165–1179, doi:10.1046/j.1365-246X.2007.03415.x.

Blewitt, G. (2007), GPS and space-based geodetic methods, in *Treatise on Geophysics*, vol. 3, *Geodesy*, edited by G. Schubert, pp. 351–390, Elsevier, Amsterdam, doi:10.1016/B978-044452748-6.00058-4.

Bonforte, A., A. Ferretti, C. Prati, G. Puglisi, and F. Rocca (2002), Calibration of atmospheric effects on sar interferograms by GPS and local atmospheric models: First results, *J. Atmos. Sol. Terr. Phys.*, *63*(12), 1343–1357, doi:10.1016/S1364-6826(00)00252-2.

Bürgmann, R., P. Rosen, and E. Fielding (2000), Synthetic Aperture Radar interferometry to measure Earth's surface topography and its deformation, *Annu. Rev. Earth Planet. Sci.*, *28*, 169–209, doi:10.1146/annurev.earth.28.1.169.

Camacho, A. G., F. Montesinos, R. Vieira, and J. Arnoso (2001), Modelling of crustal anomalies of Lanzarote (Canary Islands) in light of gravity data, *Geophys. J. Int.*, *147*(2), 403–414, doi:10.1046/j.0956-540X.2001.01546.x.

Carracedo, J., E. Rodríguez Badiola, and V. Soler (1990), Aspectos volcanológicos y estructurales, evolución petrológica e implicaciones en riesgo volcánico de la erupción de 1730 en Lanzarote, Islas Canarias, *Estud. Geol.*, *46*(1–2), 25–55, doi:10.3989/egeol.90461-2.

Casu, F., M. Manzo, and R. Lanari (2006), A quantitative assessment of the SBAS algorithm performance for surface deformation retrieval from DInSAR data, *Remote Sens. Environ.*, *102*(3–4), 195–210, doi:10.1016/j.rse.2006.01.023.

Cavalié, O., M.-P. Doin, C. Lasserre, and P. Briole (2007), Ground motion measurement in the Lake Mead area, Nevada, by differential synthetic aperture radar interferometry time series analysis: Probing the lithosphere rheological structure, *J. Geophys. Res.*, *112*, B03403, doi:10.1029/2006JB004344.

Correig, A. M., and J. Vila (1993), On the frequency contents of local events: Source or path effect?, *Geophys. J. Int.*, *115*(3), 863–877, doi:10.1111/j.1365-246X.1993.tb01498.x.

Curlander, J., and R. McDonough (1991), *Synthetic Aperture Radar: Systems and Signal Processing*, John Wiley, New York.

Dawson, J., and P. Tregoning (2007), Uncertainty analysis of earthquake source parameters determined from InSAR: A simulation study, *J. Geophys. Res.*, *112*, B09406, doi:10.1029/2007JB005209.

Delacourt, C., P. Briole, and J. Achache (1998), Tropospheric corrections of SAR interferograms with strong topography: Application to Etna, *Geophys. Res. Lett.*, *25*(15), 2849–2852, doi:10.1029/98GL02112.

Doin, M.-P., C. Lasserre, G. Peltzer, O. Cavalié, and C. Doubre (2009), Corrections of stratified tropospheric delays in SAR interferometry: Validation with global atmospheric models, *J. Appl. Geophys.*, *69*, 35–50, doi:10.1016/j.jappgeo.2009.03.010.

Dzurisin, D. (2007), *Volcano Deformation: Geodetic Monitoring Techniques*, Praxis, Chicheter, U. K.

Efron, B. (1979), Bootstrap methods: Another look at the jacknife, *Ann. Stat.*, *7*(7), 1–26, doi:10.1214/aos/1176344552.

Elliott, J., J. Biggs, B. Parsons, and T. Wright (2008), InSAR slip rate determination on the Altyn Tagh Fault, northern Tibet, in the presence of topographically correlated atmospheric delays, *Geophys. Res. Lett.*, *35*, L12309, doi:10.1029/2008GL033659.

Emardson, T., M. Simons, and F. Webb (2003), Neutral atmospheric delay in interferometric synthetic aperture radar applications: Statistical description and mitigation, *J. Geophys. Res.*, *108*(B5), 2231, doi:10.1029/2002JB001781.

Fernández, J., R. Vieira, J. Díez, and C. Toro (1992), Investigations on crustal thickness, heat flow and gravity tide relationship in Lanzarote island, *Phys. Earth Planet. Int.*, *74*(3–4), 199–208, doi:10.1016/0031-9201(92)90010-S.

Fernández, J., et al. (2009), Gravity-driven deformation of Tenerife measured by InSAR time series analysis, *Geophys. Res. Lett.*, *36*, L04306, doi:10.1029/2008GL036920.

Ferretti, A., C. Prati, and F. Rocca (2000), Nonlinear subsidence rate estimation using permanent scatterers in differential SAR interferometry, *IEEE Trans. Geosci. Remote Sens.*, *38*(5), 2202–2212, doi:10.1109/36.868878.

Fialko, Y., and M. Simons (2000), Deformation and seismicity in the Coso geothermal area, Inyo county, California: Observations and modeling using satellite radar interferometry, *J. Geophys. Res.*, *105*, 21,781–21,794, doi:10.1029/2000JB900169.

Fialko, Y., and M. Simons (2001), Finite source modelling of magmatic unrest in Socorro, New Mexico, and Long Valley, California, *Geophys. J. Int.*, *146*(1), 191–200, doi:10.1046/j.1365-246X.2001.00453.x.

Fialko, Y., D. Sandwell, M. Simons, and P. Rosen (2005), Three-dimensional deformation caused by the Bam, Iran, earthquake and the origin of shallow slip deficit, *Nature*, *435*, 295–299, doi:10.1038/nature03425.

Fornaro, G., M. Manunta, F. Serafino, P. Berardino, and E. Sansosti (2005), Advances in multipass SAR image registration, paper presented at International Geoscience and Remote Sensing Symposium, Seoul, South Korea, 25–29 July.

Foster, J., B. Brooks, T. Cherubini, C. Shacat, and S. B. C. Werner (2006), Mitigating atmospheric noise for InSAR using a high resolution weather model, *Geophys. Res. Lett.*, *33*, L16304, doi:10.1029/2006GL026781.

Goldstein, R. M. (1995), Atmospheric limitations to repeat-track radar interferometry, *Geophys. Res. Lett.*, *22*(18), 2517–2520, doi:10.1029/95GL02475.

González, P. J., K. F. Tiampo, A. G. Camacho, and J. Fernández (2010), Shallow flank deformation at Cumbre Vieja volcano (Canary Islands): Implications on the stability of steep-sided volcano flanks at oceanic islands, *Earth Planet. Sci. Lett.*, *297*(3–4), 545–557, doi:10.1016/j.epsl.2010.07.006.

Hanssen, R. (1998), Assessment of the role of atmospheric heterogeneities in ERS tandem SAR interferometry, report, Delft Inst. Earth-Oriented Space Res., Delft, Netherlands.

Hanssen, R. (2001), *Radar Interferometry: Data Interpretation and Error Analysis*, 308 pp., Kluwer Acad., Dordrecht, Netherlands.

Hanssen, R., and S. Usai (1997), Interferometric phase analysis for monitoring slow deformation processes, in *Third ERS Symposium—Space at the Service of Our Environment, Florence, Italy, 17–21 March 1997*, *Eur. Space Agency Spec. Publ.*, *ESA SP-414*, 487–491.

Hanssen, R., T. Weckwerth, H. Zebker, and R. Klees (1999), High-resolution water vapor mapping from interferometric radar measurements, *Science*, *283*, 1295–1297, doi:10.1126/science.283.5406.1297.

Hofmann-Wellenhof, B., H. Lichtenegger, and E. Wasle (2007), *GNSS-Global Navigation Satellite Systems: GPS, Glonass, Galileo, and More*, Springer, New York.

Hooper, A. (2008), A multi-temporal InSAR method incorporating both persistent scatterer and small baseline approaches, *Geophys. Res. Lett.*, *35*, L16302, doi:10.1029/2008GL034654.

Hooper, A., H. Zebker, P. Segall, and B. Kampes (2004), A new method for measuring deformation on volcanoes and other non-urban areas using InSAR persistent scatterers, *Geophys. Res. Lett.*, *31*, L23611, doi:10.1029/2004GL021737.

Hooper, A., P. Segall, and H. Zebker (2007), Persistent scatterer InSAR for crustal deformation analysis, with application to Volcán Alcedo, Galápagos, *J. Geophys. Res.*, *112*, B07407, doi:10.1029/2006JB004763.

Isaaks, E., and R. Srivastava (1989), *An Introduction to Applied Geostatistics*, Oxford Univ. Press, New York.

Just, D., and R. Bamler (1994), Phase statistics of interferograms with applications to synthetic aperture radar, *Appl. Opt.*, *33*(20), 4361–4368, doi:10.1364/AO.33.004361.

Kampes, B. M., R. F. Hanssen, and Z. Perski (2003), Radar interferometry with public domain tools, in Third International Workshop on ERS SAR Interferometry, 'FRINGE03', Frascati, Italy, 1–5 Dec.

Knospe, S., and S. Jonsson (2010), Covariance estimation for dInSAR surface deformation measurements in the presence of anisotropic atmospheric noise, *IEEE Trans. Geosci. Remote Sens.*, *48*(4), 2057–2065, doi:10.1109/TGARS.2009.2033937.

Kwoun, O.-I., Z. Lu, C. Neal, and C. Wicks (2006), Quiescent deformation of the Aniakchak Caldera, Alaska, mapped by InSAR, *Geology*, *34*(1), 5–8, doi:10.1130/G22015.1.

Lanari, R., O. Mora, M. Manunta, J. Mallorquí, P. Berardino, and E. Sansosti (2004), A small-baseline approach for investigating deformations on full-resolution differential SAR interferograms, *IEEE Trans. Geosci. Remote Sens.*, *42*(7), 1377–1386, doi:10.1109/TGRS.2004.828196.

Lee, J.-S., K. Hoppel, S. Mango, and A. Miller (1994), Intensity and phase statistics of multilook polarimetric and interferometric SAR imagery, *IEEE Trans. Geosci. Remote Sens.*, *32*(5), 1017–1028, doi:10.1109/36.312890.

Li, Z., J.-P. Muller, P. Cross, and E. Fielding (2005), Interferometric synthetic aperture radar (InSAR) atmospheric correction: GPS, moderate resolution imaging spectroradiometer (MODIS), and InSAR integration, *J. Geophys. Res.*, *110*, B03410, doi:10.1029/2004JB003446.

Li, Z., E. Fielding, P. Cross, and J.-P. Muller (2006), Interferometric synthetic aperture radar atmospheric correction: GPS topography-dependent turbulence model, *J. Geophys. Res.*, *111*, B02404, doi:10.1029/2005JB003711.

Lohman, R., and M. Simons (2005), Some thoughts on the use of InSAR data to constrain models of surface deformation: Noise structure and data downsampling, *Geochem. Geophys. Geosyst.*, *6*, Q01008, doi:10.1029/2004GC000813.

Lundgren, P., S. Usai, E. Sansosti, R. Lanari, M. Tesauro, G. Fornaro, and P. Berardino (2001), Modeling surface deformation observed with synthetic aperture radar interferometry at Campi Flegrei caldera, *J. Geophys. Res.*, *106*, 19355–19366, doi:10.1029/2001JB000194.

Lyons, S., and D. Sandwell (2003), Fault creep along the southern San Andreas from InSAR, permanent scatterers, and stacking, *J. Geophys. Res.*, *108*(B1), 2047, doi:10.1029/2002JB001831.

Massonnet, D., and K. Feigl (1998), Radar interferometry and its application to changes in the Earth's surface, *Rev. Geophys.*, *36*(4), 441–500, doi:10.1029/97RG03139.

Massonnet, D., M. Rossi, C. Carmona, F. Adagna, G. Peltzer, K. Feigl, and T. Rabaute (1993), The displacement field of the Landers earthquake mapped by radar interferometry, *Nature*, *364*, 138–142, doi:10.1038/364138a0.

Massonnet, D., P. Briole, and A. Arnaud (1995), Deflation of Mount Etna monitored by spaceborne radar interferometry, *Nature*, *375*, 567–570, doi:10.1038/375567a0.

Meyer, F., R. Bamler, N. Jakowski, and T. Fritz (2006), The potential of low-frequency sar systems for mapping ionospheric tec distributions, *Geosci. Remote Sens. Lett.*, *3*(4), 560–564, doi:10.1109/LGRS.2006.882148.

Middleton, G., and P. Wilcock (1994), *Mechanics in the Earth and Environmental Sciences*, 459 pp., Cambridge Univ. Press, New York.

Mogi, K. (1958), Relations between eruptions of various volcanoes and the deformation of the ground surface around them, *Bull. Earthquake Res. Inst. Univ. Tokyo*, *36*, 99–134.

Mora, O., J. Mallorquí, and A. Broquetas (2003), Linear and non-linear terrain deformation maps from a reduced set of interferometric SAR images, *IEEE Trans. Geosci. Remote Sens.*, *41*(10), 2243–2253, doi:10.1109/TGRS.2003.814657.

Onn, F., and H. Zebker (2006), Correction for interferometric synthetic aperture radar atmospheric phase artifacts using time series of zenith wet delay observations from a GPS network, *J. Geophys. Res.*, *111*, B09102, doi:10.1029/2005JB004012.

Palano, M., M. Rossi, F. Cannavo, V. Bruno, M. Aloisi, D. Pellegrino, M. Pulvirenti, G. Siligato, and M. Mattia (2010), Etn@ref: a geodetic reference frame for Mt. Etna GPS networks, *Ann. Geophys.*, *53*(4), 49–57, doi:10.4401/ag-4879.

Peltzer, G., P. Rosen, F. Rogez, and K. Hudnut (1996), Postseismic rebound in fault step-overs caused by pore fluid flow, *Science*, *273*, 1202–1204, doi:10.1126/science.273.5279.1202.

Perlock, P., P.J. González, K. Tiampo, G. Rodríguez-Velasco, S. Samsonov, and J. Fernández (2008), Time evolution of deformation using time series of differential interferograms: Application to La Palma Island (Canary Islands), *Pure Appl. Geophys.*, *165*(8), 1531–1554, doi:10.1007/s00024-004-0388-7.

Puysségur, B., R. Michel, and J.-P. Avouac (2007), Tropospheric phase delay in InSAR estimated from meteorological model and multispectral imagery, *J. Geophys. Res.*, *112*, B05419, doi:10.1029/2006JB004352.

Rodriguez, E., and J. Martin (1992), Theory and design of interferometric synthetic-aperture radars, *IEE Proc., F*, *139*(2), 147–159.

Romero, R., D. Carrasco, V. Araña, and J. Fernández (2003), A new approach to the monitoring of deformation on Lanzarote (Canary Islands): An 8-year perspective, *Bull. Volcanol.*, *65*, 1–7, doi:10.1007/s00445-002-0232-3.

Saastamoinen, J. (1972), Introduction to practical computation of astronomical refraction, *Bull. Geod.*, *106*, 383–397, doi:10.1007/BF02522047.

Scharroo, R., and P. Visser (1998), Precise orbit determination and gravity field improvement for the ERS satellites, *J. Geophys. Res.*, *103*, 8113–8127, doi:10.1029/97JC03179.

Schmidt, D. A., and R. Bürgmann (2003), Time-dependent land uplift and subsidence in the Santa Clara valley, California, from a large interferometric synthetic aperture radar data set, *J. Geophys. Res.*, *108*(B9), 2416, doi:10.1029/2002JB002267.

Simons, M., and P. A. Rosen (2007), Interferometric synthetic aperture radar geodesy, in *Treatise on Geophysics*, vol. 3, *Geodesy*, edited by G. Schubert, pp. 391–446, Elsevier, Amsterdam, doi:10.1016/B978-044452748-6.00059-6.

Simons, M., Y. Fialko, and L. Rivera (2002), Coseismic deformation from the 1999 M_w 7.1 Hector Mine, California, earthquake as inferred from InSAR and GPS observations, *Bull. Seismol. Soc. Am.*, *92*(4), 1390–1402, doi:10.1785/0120000933.

Strozzi, T., U. Wegmüller, L. Tosi, G. Bitelli, and V. Spreckels (2001), Land subsidence monitoring with differential SAR interferometry, *Photogramm. Eng. Remote Sens.*, *67*(11), 1261–1270.

Sudhaus, H., and S. Jonsson (2009), Improved source modeling through combined use of InSAR and GPS under consideration of correlated data errors: Application to the June 2000 Kleifarvatn earthquake Iceland, *Geophys. J. Int.*, *176*(2), 389–404, doi:10.1111/j.1365-246X.2008.03989.x.

Tatarski, V. (1961), *Wave Propagation in a Turbulent Medium*, translated from Russian, McGraw-Hill, New York.

Teunissen, P. (2003), *Adjustment Theory: An Introduction*, *Math. Geod. Position. Ser.*, vol. 24, 2 ed., 193 pp., VSSD, Delft, Netherlands.

Teunissen, P. (2006), *Testing Theory: An Introduction*, *Math. Geod. Position. Ser.*, 1 ed., 147 pp., VSSD, Delft, Netherlands.

Tizzani, P., P. Berardino, F. Casu, P. Euillades, M. Manzo, G. Ricciardi, G. Zeni, and R. Lanari (2007), Surface deformation of Long Valley caldera and Mono Basin, California investigated with the SBAS-InSAR approach, *Remote Sens. Environ.*, *108*(3), 277–289, doi:10.1016/j.rse.2006.11.015.

Usai, S. (1997), The use of man-made features for long time scale InSAR, paper presented at International Geoscience and Remote Sensing Symposium, Singapore, 3–8 Aug.

Usai, S. (2003), A least squares database approach for SAR interferometric data, *IEEE Trans. Geosci. Remote Sens.*, *41*(4), 753–760, doi:10.1109/TGRS.2003.810675.

Usai, S., and R. Hanssen (1997), Long time scale InSAR by means of high coherence features, in *Third ERS Symposium—Space at the Service of Our Environment, Florence, Italy, 17–21 March 1997*, *Eur. Space Agency Spec. Publ.*, *ESA SP-414*, 225–228.

Vanicek, P., and E. Krakiwsky (1986), *Geodesy: The Concepts*, 2nd ed., 697 pp., North-Holland, Amsterdam.

Wadge, G., et al. (2002), Atmospheric models, GPS and InSAR measurements of the tropospheric water vapour field over mount etna, *Geophys. Res. Lett.*, *29*(19), 1905, doi:10.1029/2002GL015159.

Williams, S., Y. Bock, and P. Fang (1998), Integrated satellite interferometry: Tropospheric noise, GPS estimates and implications for interferometric synthetic aperture radar products, *J. Geophys. Res.*, *103*, 27,051–27,067, doi:10.1029/98JB02794.

Zebker, H., and J. Villasenor (1992), Decorrelation in interferometric radar echoes, *IEEE Trans. Geosci. Remote Sens.*, *30*(5), 950–959, doi:10.1109/36.175330.

Zebker, H., P. Rosen, and S. Hensley (1997), Atmospheric effects in interferometric synthetic aperture radar surface deformation and topographic maps, *J. Geophys. Res.*, *102*, 7547–7563, doi:10.1029/96JB03804.

J. Fernández, Instituto de Geociencias, Facultad de Ciencias Matemáticas, CSIC-Universidad Complutense de Madrid, Plaza de Ciencias 3, Ciudad Universitaria, Madrid E-28040, Spain. (jft@mat.ucm.es)

P. J. González, Department of Earth Sciences, University of Western Ontario, Biological and Geological Sciences Building, London, ON N6A 5B7, Canada. (pabloj.glez@gmail.com)